The effects of structural integrity of graphene on the thermoelectric properties of the n-type bismuth-telluride alloy

Farah M. El-Makaty[a], K. Andre Mkhoyan[b], Khaled M. Youssef[a,*]

[a] *Department of Materials Science and Technology, Qatar University, Doha 2713, Qatar*
[b] *Department of Chemical Engineering and Materials Science, University of Minnesota, Minneapolis 55455, MN, USA*

ARTICLE INFO

ABSTRACT

This study examines the effects of the structural integrity of graphene on the thermoelectric properties of n-type bismuth telluride alloy. Graphene/$Bi_2Te_{2.7}Se_{0.3}$ composites were prepared via mechanical alloying and spark plasma sintering techniques. Different graphene concentrations (0.05 and 0.5 wt%) and addition times (20 hrs, 10 mins, and 1 min) were considered. The thermoelectric properties were measured, and the results showed that the milling time affects graphene structure as well as its agglomeration. It is revealed that the optimum time to add the two-dimensional filler is during the last phase of mechanical milling as it will preserve graphene's structure and boost the electrical conductivity. It is also shown that as the milling time of graphene increases, the Seebeck coefficient improves. Even though an increase in the thermal conductivity is expected due to the high electrical conductivity, a clear reduction in the lattice thermal conductivity part was obtained due to the increased scattering at the new interfaces. The figure-of-merit for the optimum sample with 0.05 wt% graphene added in the last 10 mins of milling had an improvement of 19% at room temperature reaching a value of 0.5, and 25% at 160 °C achieving a final value of 0.81.

1. Introduction

One of the current state-of-the-art thermoelectric materials (TE) used for near room-temperature applications is the bismuth-telluride system. The exclusive thermoelectric properties of bismuth telluride are due to its layered structure [1,2]. This structure results in high mobility of charge carriers (weighted mobility of 525 cm^2/V.s), accompanied by a low lattice thermal conductivity (~1.37 W/m K), making it a promising thermoelectric material [3]. Doping bismuth telluride with selenium ($Bi_2(Te_{1-\delta}Se_\delta)_3$) gives electron conducting material (n-type), and the optimized composition corresponding to the highest figure-of-merit (ZT) and a low bandgap is well-documented to be $Bi_2Te_{2.7}Se_{0.3}$ [4]. However, the applications of $Bi_2(Te_{1-\delta}Se_\delta)_3$ as a TE is greatly restricted by the low performance of ZT≈ 1 at room temperature [4,5]. Addition of nanofillers to n-type bismuth telluride matrix is one way to improve its thermoelectric properties. Kyung et al. [6] prepared MWCNT-$Bi_2Te_{2.7}Se_{0.3}$ composite via poly-reduction method and improved the ZT from 0.28 to 0.51 at room temperature. Kim et al. [7] improved the ZT by 17% by adding Al_2O_3 to n-type $Bi_2(Te_{0.9}Se_{0.1})_3$.

Graphene is the most well-known two-dimensional filler that has remarkably high thermal and electrical properties reaching up to 2800 W/m.K and 200 S/m, respectively [8]. It has a zero-band gap, high charge carriers concentration and a mobility of ~200,000 cm^2/V.s [9]. In addition, the mechanical properties of graphene accounts as a further outstanding advantage. The theoretical values for the tensile strength and Young's modulus are 130 GPa and 1 TPa, respectively, which are among the highest of all materials discovered so far [10]. Many factors can affect graphene's behavior as a nanofiller, including its amount, uniformity, and structural integrity. Possessing a very brittle structure, it is important to assure graphene's structural integrity during the preparation process [11].

The effect of using graphene as a nanofiller for n-type bismuth telluride alloy has been limitedly addressed. Agarwal et al. [12] mixed Bi_2Te_3 powder with 0.05 wt% graphene using agate mortar and pestle and showed improvements in ZT value. Kumar et al. [13] also proved the ability of graphene in enhancing the ZT value upon addition to Bi_2Te_3 nanosheets through reflexing method. Jin et al. [9] prepared unoxidized graphene/$Bi_2Te_{2.7}Se_{0.3}$ composite through chemical reduction method and showed improvements in ZT for both as-exfoliated and ultrasonicated matrixes. Other studies examined the effect of different graphene concentrations (up to 10 wt%) via wet-chemical synthesis methods [14–16] and ball milling [17]. However, up to our knowledge, there are no studies that show the

---

* Corresponding author.
E-mail address: Kyoussef@qu.edu.qa (K.M. Youssef).

effect of graphene's structural integrity on the thermoelectric properties of $Bi_2Te_{2.7}Se_{0.3}$.

This paper utilizes ball milling as a preparation technique to study the effect of graphene structural integrity on the thermoelectric properties of n-type $Bi_2Te_{2.7}Se_{0.3}$ alloy. This is done by preparing several composites where graphene nanoplatelets (GNPs) are added in different amounts and during various timings of the mechanical milling process. The thermoelectric properties of each sample are examined and compared to a pristine bismuth telluride alloy prepared using the same conditions.

2. Experimental

2.1. Materials and synthesis of GNP-$Bi_2Te_{2.7}Se_{0.3}$ composites

Elemental powder of bismuth (99.999%), selenium (99.5%), and tellurium (99.99%) from Alfa Aesar were used to prepare the n-type bismuth telluride alloy of a composition $Bi_2Te_{2.7}Se_{0.3}$. The powders were loaded in a stainless-steel vial under an ultra-high purity argon atmosphere ($O_2 < 0.5$ ppm) and milled with a ball-to-powder weight ratio of 7:1 for 20 h using an SPEX milling device (SamplePrep, 8000 M). In order to investigate the effect of milling on the structural integrity of GNPs and the corresponding thermoelectric properties, GNPs from Sigma-Aldrich were added to different patches of the $Bi_2Te_{2.7}Se_{0.3}$ at various milling time intervals (at the beginning of ball milling; at the last ten minutes; and the last one minute). Accordingly, four different GNP-$Bi_2Te_{2.7}Se_{0.3}$ composites of different GNP concentrations and addition milling time were prepared using the same milling conditions of the pristine $Bi_2Te_{2.7}Se_{0.3}$. A list of the prepared samples and their milling time conditions is shown in Table 1. Consolidation of the milled powders was carried out using a Spark Plasma Sintering (SPS) technique. The milled powders were loaded into a 12.7 mm graphite die and then compacted via SPS at a pressure of 45 MPa and a temperature of 400 °C for a holding time of 10 min under a nitrogen atmosphere.

2.2. Characterization

Phase identification of the as milled powder and compacted samples were investigated via X-ray diffraction (XRD: PANalytical, EMPYREAN), using Cu/Kα radiation source and a wavelength of 1.54 Å. The degree of crystallinity and structural defects of GNPs were examined by Raman Spectroscopy (RS: Thermo Fisher, DXR) using a wavelength of 532 nm and a laser power of 10 mW. The surface morphology of milled powders was analyzed by Scanning Electron Microscopy (SEM: Nano-SEM Nova 450, FEI-USA). The transmission electron microscopy (TEM) analysis was used to investigate the microstructure features and the grain size of the processed samples. The TEM analyses were carried out using an FEI Titan™ 60–300 TEM. The TEM sample preparation was performed using a focused ion beam (FEI Helios NanoLab™ G4 FIB/SEM) dual system.

For the measurements of the thermoelectric properties, the Seebeck coefficient and the electrical conductivity of the consolidated discs (12.7 mm in diameter and 3 mm in thickness) were measured simultaneously using the SBA 485 Nemesis – NETZSCH. The thermal conductivity was measured using an LFA 467 Hyper

Flash device – NETZSCH. These measurements were performed under UHP argon atmosphere in a temperature range of 25–300 °C295–573 K. The measurements for each sample was repeated three times, and the error bar was less than 7%. The density of the consolidated discs was measured based on the Archimedes principle using the Sartorius density determination kit (Sartorius YDK03, Germany). The density determination kit was set up using distilled water, and the water's temperature was monitored during the measurement. For all the samples, the relative density was found to be above 99%.

3. Results and discussion

The XRD results of the as milled powders for pristine and GNP-composite samples are shown in Fig. 1a. All peaks match the X-ray diffraction (reference code 98–024–7619) for doped n-type bismuth telluride [18]. No graphene peaks were present in the diffraction patterns since it was only added in small amounts. The grain size was calculated using the Warren-Averbach model [19]:

$$\frac{\beta_{hkl}^2}{\tan^2\theta} = \frac{\lambda}{D}\left(\frac{\beta_{hkl}}{\tan\theta\sin\theta}\right) + 25\langle\varepsilon^2\rangle \tag{1}$$

where β_{hkl} is the width of the peak at half-maximum intensity, λ is the wavelength of the x-ray beam, θ is the peak position, D is the average grain size, and ε is the lattice strain. Fitting $\beta_{hkl}^2/\tan^2\theta$ vs $\beta_{hkl}/(\tan\theta\sin\theta)$ gave a linear regression fit of at least 0.8 for all measurements. The grain size for as milled powders ranged from 17 to 19 nm (Table 2). Fig. 1b shows the XRD patterns of the same samples after the SPS consolidation. It is observed that the XRD peaks became narrower after the SPS, implying an increase in the grain size. According to Eq. (1), the average grain size values of the consolidated samples after the SPS range from 38 to 51 nm (see Table 2). The increase in grain size is mainly due to the high temperature used during compaction [20]. These XRD patterns are in good agreement with the reported XRD of the as milled Bi_2Te_3 powders and furnace sintered discs reported by Ahmed et. al [17].

Fig. 2a shows the bright-field TEM image of the as milled 0.05GNP-10 m sample. It can be seen that the grains are equiaxed and randomly distributed within the structure. The average grain size was calculated from several dark-field TEM images (see Fig. 2b), and the corresponding grain size distribution is shown in Fig. 2c. The average grain size of the 0.05GNP-10 m sample is 19 ± 6 nm with no grains above 50 nm. This grain size value is similar to that determined from the XRD data and comparable with the reported values. Zhang et al. [21] reported a grain size of 10 nm for p-type graphene/$Bi_{0.4}Sb_{1.6}Te_3$ prepared by milling and high-pressure sintering. The electron diffraction pattern shown in Fig. 2d reveals the atomic planes of the pseudohexagonal $Bi_2Te_{2.7}Se_{0.3}$ nanograins, matching well with the XRD patterns. To investigate the distribution of graphene in the as milled 0.05GNP-10 m sample, high-angle annular dark-field (HAADF) STEM imaging with EDS elemental mapping was performed. As shown in Fig. 3, the distribution of Bi, Te, Se, and C is uniform throughout the sample. After the consolidation of the as milled 0.05GNP-10 m sample using the spark plasma sintering technique, the grain size increases due to the heat of the sintering process. Fig. 4a shows a bright-field TEM image for the consolidated 0.05GNP-10 m sample along with the corresponding electron diffraction pattern (Fig. 4b). The grain size increases after sintering; however, most of the grains are in the range of 50–120 nm.

Fig. 5 shows the SEM images of the morphologies for the as milled powder samples and the as-received GNPs. Fig. 5a, reveals the typical two-dimensional layered graphene nanosheets. The pristine $Bi_2Te_{2.7}Se_{0.3}$ in Fig. 5b shows the milled powder with different particle sizes. The GNPs were present and marked with red arrows in samples 0.5GNP-10 m, 0.05GNP-1 m, and 0.05GNP-10 m, see Fig. 5c,
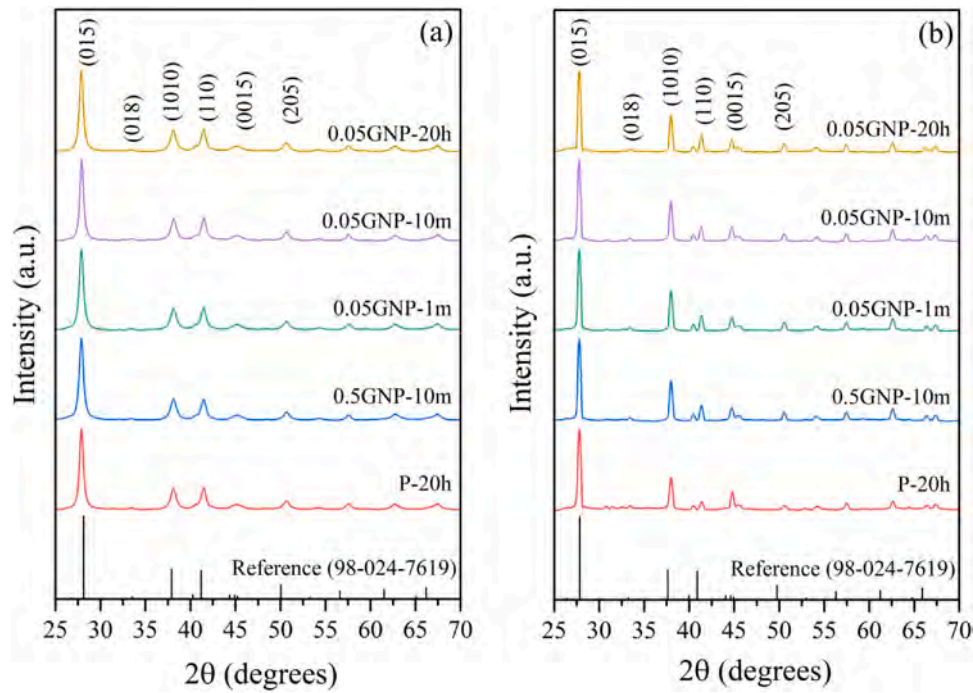
Table 1
List of samples prepared with different GNP concentrations and addition time.

Sample Code	GNP amount (wt%)	GNP addition time
P-20 h	0	–
0.05GNP–20 h	0.05%	at the beginning
0.05GNP–10 m	0.05%	last 10 min
0.5GNP–10 m	0.5%	last 10 min
0.05GNP–1 m	0.05%	last 1 min

Fig. 1. XRD patterns for pristine and GNP-$Bi_2Te_{2.7}Se_{0.3}$ composites (a) as milled powder and (b) spark plasma sintered discs, and the reference card 98–024–7619 for $Bi_2Te_1Se_2$.

Table 2
Grain sizes evaluated using Warren-Averbach calculations for pristine and GNP-BiTeSe nanocomposite samples.

Sample Code	Grain Size (nm)	
	As milled powder	Spark plasma sintered discs
P-20 hrs	19	38
0.5GNP-10 m	17	44
0.05GNP-1 m	18	40
0.05GNP-10 m	18	45
0.05GNP-20 h	18	51

d, and e, respectively. It can be seen that a relatively high amount of GNPs was realized in the 0.5GNP-10 m sample, which exhibits a higher concentration of GNPs than that on the 0.05GNP-10 m sample. The SEM-EDS mapping of the elements in the 0.5GNP-10 m and 0.05GNP-20 h samples are shown in Figs. 6 and 7, respectively. These analyses confirm that the observed nanosheets in the 0.5GNP-10 m sample are GNPs, whereas no nanosheets of GNPs were observed in the 0.05GNP-20 h sample. The absence of nanosheets of GNPs in the 0.05GNP-20 h sample could be attributed to the extensive milling time (20 h) and the severe plastic deformation causing fragmentation of the GNPs. Ahmed et al. [17] studied the morphology of undoped n-type Gr/Bi_2Te_3 revealing agglomerated particles with clear graphene nanosheet morphologies and described the Bi_2Te_3 particles being wrapped by graphene nanosheets. Similarly, Liang et al. [14] described their composite by a large number of graphene nanosheets coated around Bi_2Te_3 particles. However, it is noticed in our samples that the GNPs are located in-between or on top of the matrix particles with variation in nanolayer thickness.

Raman spectroscopy analysis was performed to further examine the structural variations of the GNPs in the milled samples. Fig. 8 shows the Raman spectroscopy results for the GNPs in the composite samples compared to the as-received GNPs. The spectra exhibit the G and 2D characteristic bands of graphene [5,24]. The D band appears in all examined samples reflecting a level of defects within the carbon lattice of the as-received GNPs. Table 3 shows the calculated intensity ratio, I_G/I_D, which provides an estimation for the GNPs

structural integrity. The highest I_G/I_D ratio (6.5) is for the as-received GNPs, followed by a slightly lower value of 6.4 for the sample where the GNPs were added at the last minute of the mechanical milling. This suggests that GNP's crystal structure in this sample was preserved. These results are in good agreement with the data reported by Li et. al [22], where p-type $Bi_{0.4}Sb_{1.6}Te_3$ was blended with graphene in water and acetone, and the Raman Spectra displayed a preserved crystal structure of graphene. The I_G/I_D ratio in the n-type composite gradually decreases in the samples where it was added at the last 10 min and finally diminishes to 0.7 in the sample where GNP was added at the beginning. The I_G/I_D ratio for 0.05GNP-20 h sample indicates that the crystal structure of GNP was completely lost, which may explain why no GNPs were observed during SEM analysis. The results show a clear relationship between GNP's milling time and its structural integrity, where the longer the milling time, the higher the degree of milling-induced structural defects. However, these observations only are applied to mechanical milling as the behavior of graphene will differ depending on the processing technique. For instance, Weon et al. [5] prepared p-type graphene/$Bi_{0.36}Sb_{1.64}Te_3$ composite through melt spinning process, and the I_G/I_D ratio was higher in the composite sample (1.16) compared to pristine graphene (1.06). The improved crystallinity of graphene was explained by the heat introduced during the melt spinning process.

The 2D band shows another important trend. The intensity of the band is clearly decreasing with increasing milling time, and completely diminishes in the "20 h" sample, see Fig. 8. This further confirms the loss of GNP structural integrity due to the large amount of defects introduced during mechanical milling [23]. In addition, the intensity of 2D band in the as-received GNP is much lower than the G band with an I_G/I_{2D} ratio of 2, implying that the GNPs are multi-layered and agglomerated [24,25]. This ratio did not change for 0.5GNP-10m and 0.05GNP-1m samples, indicating that GNPs here are also agglomerated and multi-layered. However, The ratio decreased to 1.7 in 0.05GNP-10m sample, suggesting the exfoliation of GNP to fewer layers [23,26]. Furthermore, the G band position provides further indication of the GNP's exfoliation. Typically, as the number of layers decreases, the G band shifts to higher Raman energies [27,28]. Compared to the as-received GNPs, the 0.05GNP-1 m
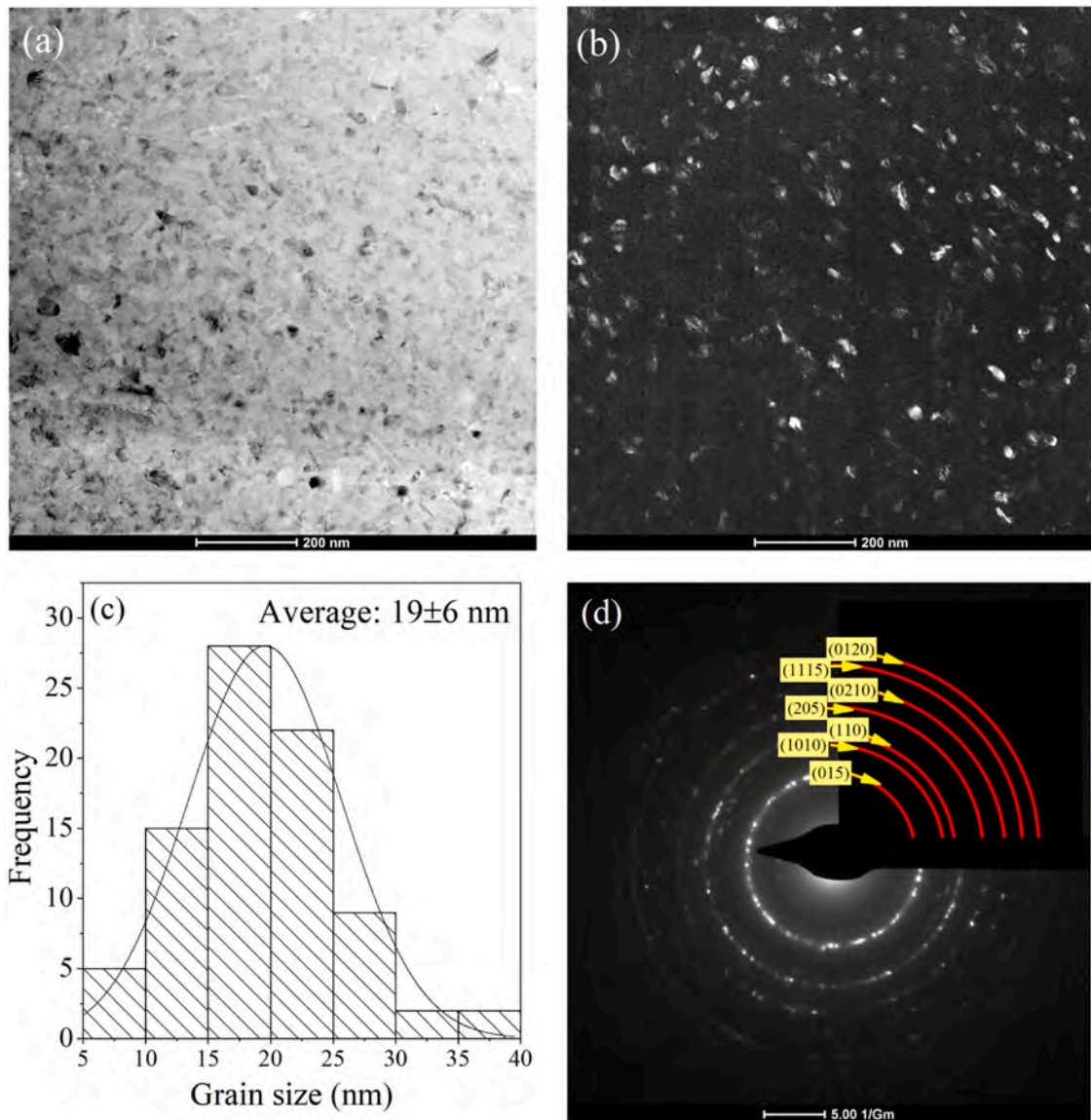
Fig. 2. (a) Bright-field TEM image, (b) dark-field TEM image (c) grain size distribution, and (d) diffraction pattern for the as milled 0.05GNP-10m sample.

sample did not have enough time to exfoliate (see Table 3). The GNPs in the 0.5GNP-10m and 0.05GNP-10 m samples had similar exfoliation extents. However, due to the higher amount of GNPs in the 0.5GNP-10m sample, agglomeration still exists, as the I_G/I_{2D} ratio suggested. The G band position is shifted the most in the 0.05GNP-20h sample, indicating higher exfoliation of GNPs than the other samples, which might be another reason for the absence of GNPs in the SEM analysis, Fig. 5f. Even though milling the GNPs for one-minute preserves its structure, it is not enough for the exfoliation to take place. Increasing the milling time to 10 min enhances the exfoliation and reduces the agglomeration only in the lower GNP concentration of 0.05 wt%. However, the structural integrity of the GNPs breaks down for long hours of milling (20 h).

Fig. 9a shows the electrical conductivity trends for the consolidated discs of the pristine and composite samples. It is shown that the electrical conductivity decreases with increasing temperature. This trend indicates a degenerate semiconductor behavior of the materials [12–14,17]. Comparing the 0.5GNP-10m and 0.05GNP-10m samples, which exhibit the exact processing conditions except for the GNPs concentration, shows that the lower concentration of GNPs results in improved electrical conductivity. High GNP content,

accompanied by agglomeration, increases the carrier scattering at the interfaces. The induced scattering lowers the charge carriers' mobility and contributes to the reduction of the electrical conductivity [5]. This result is consistent with the reported data by Shin et al. [5], Zhang et al. [21], and Dewen et al. [29] for doped p-type Gr/ BiSbTe composites. Assessing the effect of GNPs structural integrity with various milling time on the electrical conductivity is shown by comparing the results of the samples with the same content of GNPs (0.05 wt%). As can be seen from Fig. 9a, the electrical conductivity decreases with increasing the milling time of GNPs over the entire temperature range. This can be directly related to GNP's structural integrity. From Raman Spectroscopy, less milling time preserves the GNP's structure, hence preserving the GNP's high electrical properties in these samples [30]. Thus, the obtained electrical property is mainly a factor of the GNP's amount and its structural integrity. A combined optimization in these two factors led to a 45% improvement in the electrical conductivity of the samples with lower GNPs concentration (0.05%) that was added at the last phase of ball milling.

The Seebeck coefficient values for the same samples are shown in Fig. 9b. The obtained values are negative, indicating n-type
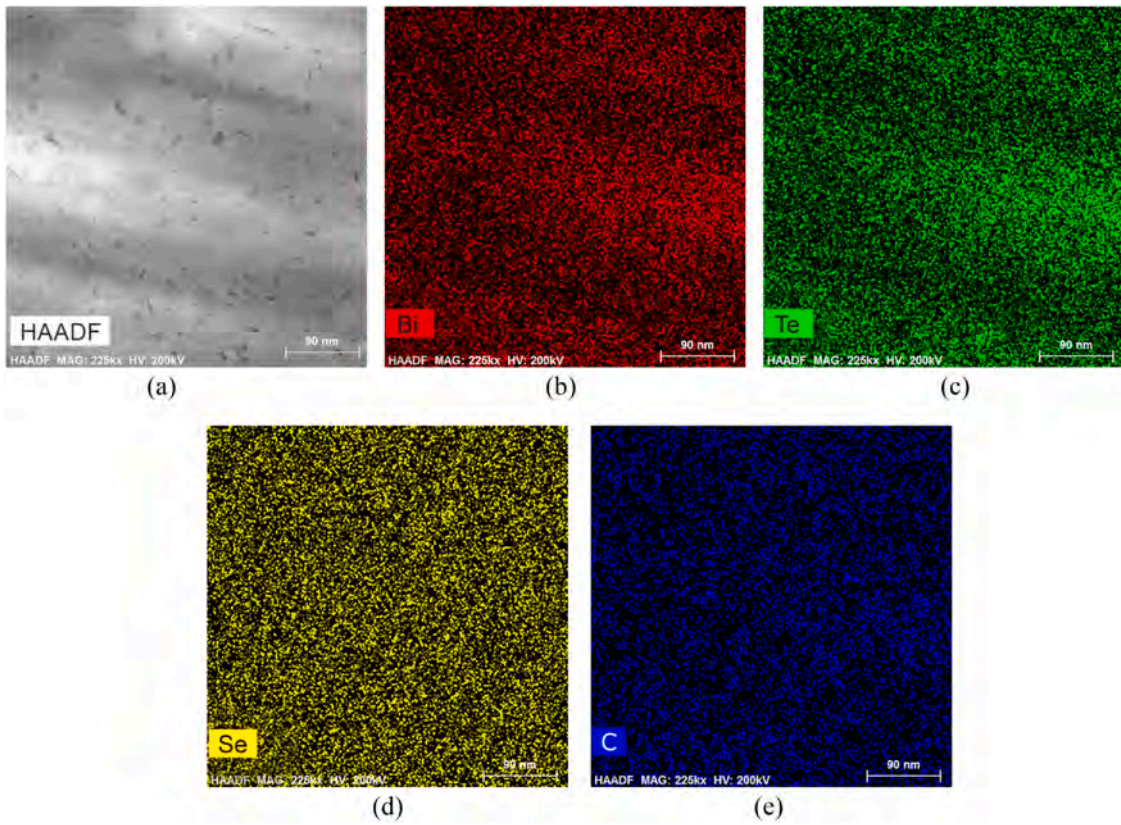
Fig. 3. HAADF-STEM image and the corresponding EDX elemental maps showing the elemental distributions of Bi, Te, Se, and C in the as milled 0.05GNP-10m sample.

thermoelectric materials. Besides, as the temperature increases, the Seebeck coefficient increases until the trend is reversed due to the bipolar effect of minority charge carriers. The maximum Seebeck achieved by all samples is at 160 °C, which agrees well with the reported data by Zhang et al. [21] for the p-type GNP-$Bi_{0.4}Sb_{1.6}Te_3$ composites. Moreover, it can be seen from Fig. 9b that the Seebeck coefficient values of the samples 0.5GNP-10m and 0.05GNP-10m are pretty similar in the range of 25–160 °C. However, lower GNPs concentration in the 0.05GNP-10m sample gives higher Seebeck coefficient values above 160 °C, which could be attributed to the better scattering and enhanced filtering of low energy carriers. This indicates that the 0.05% GNPs with less agglomeration could be the reason for the enhanced electrical and Seebeck properties.

Comparing the samples with 0.05 wt% GNP reveals a direct relationship between the Seebeck coefficient and the GNPs' milling time. It is observed here that the longer the GNPs' milling time, the higher the absolute value of the Seebeck coefficient. Mainly, the Seebeck coefficient is an intrinsic material property [1]. Hence, the stability of the GNPs through the milling process affects the structure of the final resulted material. The results show that for the same ΔT, when the GNPs were milled for the longest time, a higher thermoelectric voltage was induced [31], sample 0.05GNP-20h. This indicates that low structural integrity and more defects in GNP can result in enhancements in the Seebeck coefficient for GNP- $Bi_2Te_{2.7}Se_{0.3}$. The combined effect of the prior two parameters, represented as the power factor, is shown in Fig. 9c. The optimized
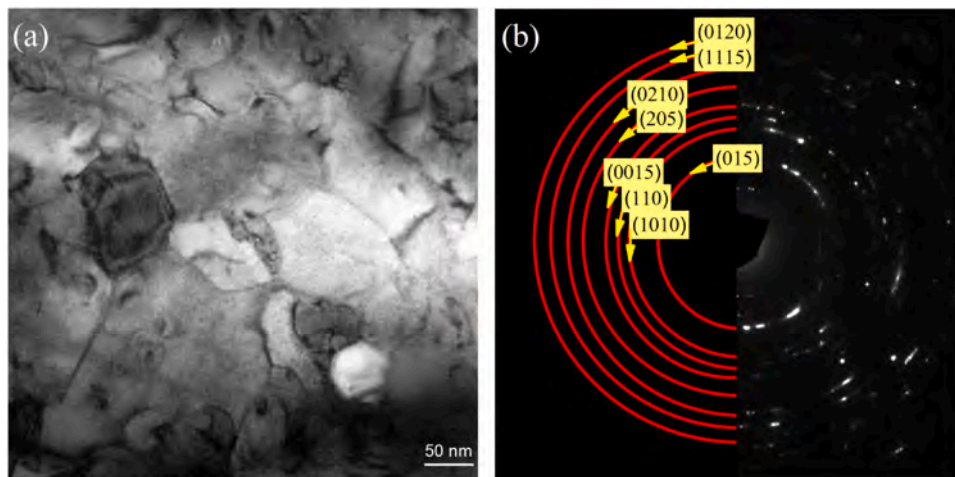

Fig. 4. (a) Bright-field TEM image of the spark plasma sintered 0.05GNP-10m sample and (b) the corresponding selected area electron diffraction pattern with the indexed rings.
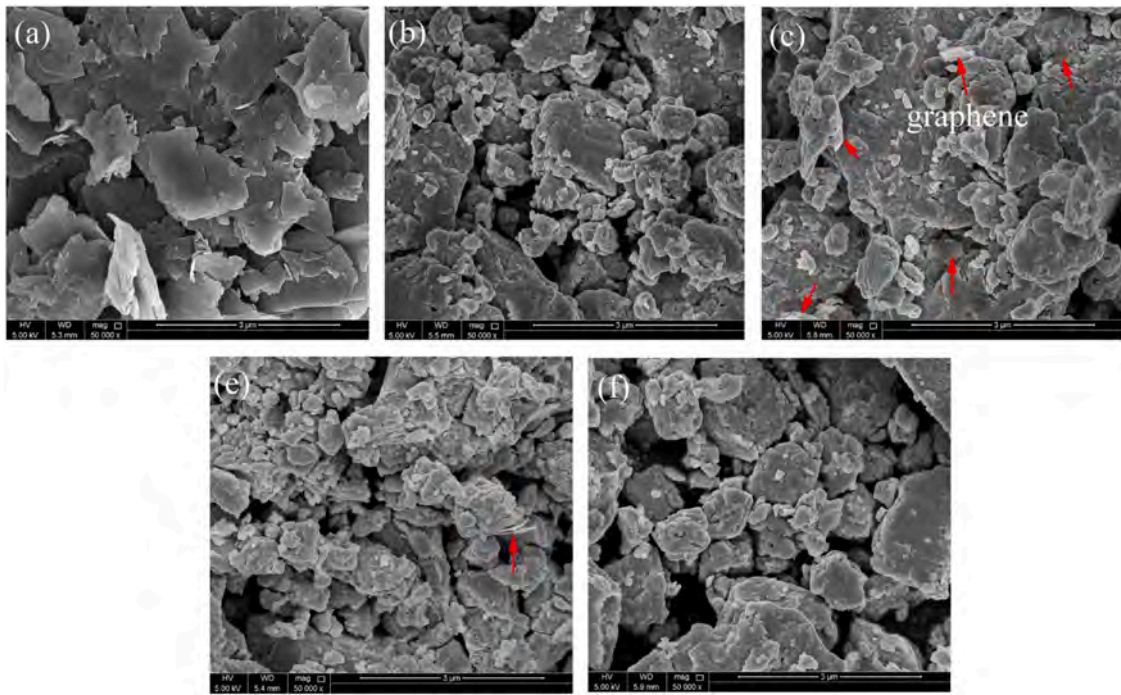
Fig. 5. SEM images for (a) as-received graphene, (b) P-20h, (c) 0.5GNP-10m, (d) 0.05GNP-1m, (e) 0.05GNP-10m and (f) 0.05GNP-20 samples.
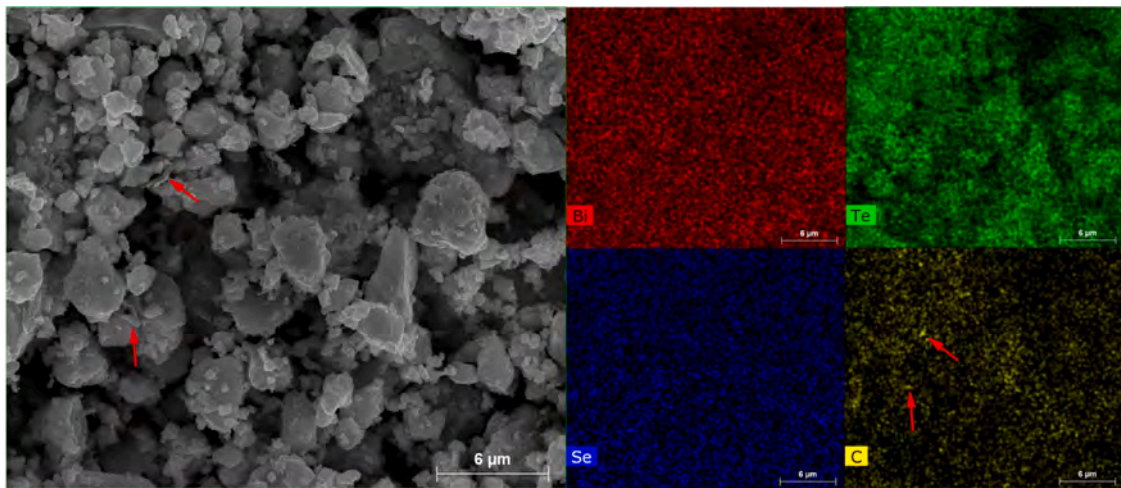

Fig. 6. SEM image with elemental mapping using EDS for milled 0.5GNP-10m sample.

two samples are the ones with lower GNPs concentration added during the last phase of mechanical milling (0.05GNP-10 m and 0.05GNP-1m).

The thermal conductivity measurements for these optimized samples were performed and compared with that of the pristine bismuth telluride sample. The results are shown in Fig. 10. It can be seen that the total thermal conductivity values of the two composite samples are higher than that of the pristine sample. This trend does not agree with most graphene-based n-type bismuth telluride, where graphene addition typically reduces their thermal conductivity due to the increased scattering at the new interfaces [12–14,17]. Therefore, the partial effect of the thermal conductivity constituents represented as the electronic (κ_E), the lattice vibration (κ_L), and the bipolar ($\kappa_{bipolar}$) thermal conductivities are calculated. The electronic thermal conductivity is calculated according to the Wiedemann-Franz law ($\kappa_e = L\sigma T$), where L is Lorenz number of $L = 2.0 \times 10^{-8}$ V^{2}K^{-2}, σ is the electrical conductivity, and T is the

measured temperature [9,21], see Fig. 10b. The summation of the lattice and bipolar thermal conductivities is calculated by subtracting the electronic component from the total thermal conductivity ($\kappa_L + \kappa_{bipolar} = \kappa_{Total} - \kappa_E$) [31] (see Fig. 10c). As presented, the overall trend of the lattice and bipolar thermal conductivities is in good agreement with the results reported in several studies [12–14,17], where the addition of a nanofiller lowers the thermal conductivity as a result of the increased scattering at the new interfaces. Moreover, the bipolar thermal conductivity for the pristine (P-20h) sample was suppressed from room temperature up to 100 ºC, as both electrons and holes are now contributing to the transportation of thermal energy. However, in the sample with enhanced GNP exfoliation (0.05GNP-10 m), the bipolar effect is suppressed for a higher temperature range (up to 140 ºC), which indicates the ability of GNP to filter the minority carriers (holes) at high temperatures. On the other hand, the electronic thermal conductivity is probably the reason for the increase in the overall thermal conductivity. This
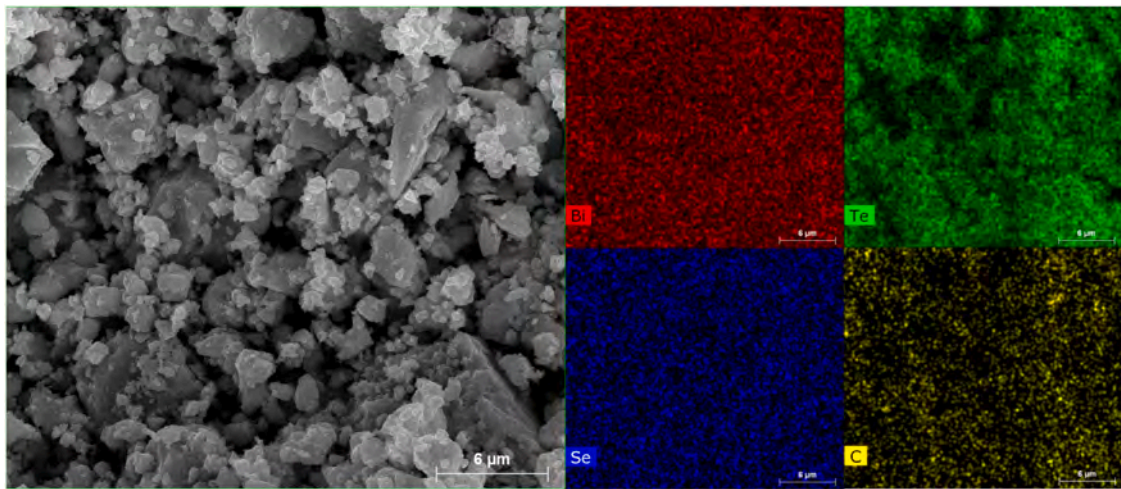
Fig. 7. SEM image with elemental mapping using EDS for milled 0.05GNP-20h sample.
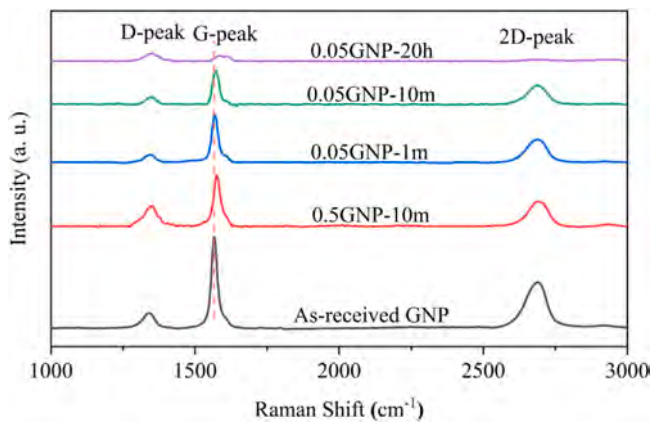

Fig. 8. Raman Shift for the GNP-Bi$_2$Te$_{2.7}$Se$_{0.3}$ composite samples.

Table 3

I$_G$/I$_D$ and I$_G$/I$_{2D}$ ratios and G band position of the prepared composites obtained from Raman Shift measurements presented in Fig. 8.

Sample	Intensity Ratio		Band Position
	I$_G$/I$_D$	I$_G$/I$_{2D}$	G
GNP	6.551	2.010	1566.8
0.5GNP-10 m	2.518	2.062	1575.8
0.05GNP-1 m	6.351	2.075	1568.8
0.05GNP-10 m	4.413	1.759	1572.9
0.05GNP-20 h	0.732	–	1583.2

is mainly because the electronic thermal conductivity part is directly proportional to electrical conductivity [21], which was high in these samples (Fig. 9a) due to the preserved structure of GNP with less agglomeration.

The figure-of-merits, shown in Fig. 10d, reveal significant enhancements in the GNP-Bi$_2$Te$_{2.7}$Se$_{0.3}$ composites. As can be seen, the ZT values of the composite samples are higher than that of the pristine bismuth telluride throughout the whole temperature range. At room temperature, the GNPs addition in the 0.05GNP-10m and 0.05GNP-1m samples improved the ZT value to be 0.45 and 0.5, respectively. Both values are higher than that of the pristine bismuth telluride (0.4). Besides, the maximum enhancement of the ZT values was obtained at a temperature of 160 °C and reached 0.81 for the 0.05GNP-10m sample. This ZT value represents about 25% enhancement above that of the pristine bismuth telluride. A comparison of these results to other studies using graphene filler along with n-type bismuth telluride mainly shows better overall improvements. Ahmed et al. [17] obtained a maximum ZT value of 0.29 at room temperature and 0.55 at 227 °C using 1 wt% reduced graphene oxide. Liang et al. [14] reached 0.21 for the figure-of-merit of the optimum sample containing 0.2 vol% reduced graphene nanosheets. Kumar et al. [13] obtained a maximum ZT of 0.35 at 70 °C using reduced graphene oxide. However, Agrawal et al. [32] prepared their composite with 0.05 wt% graphene monolayer and undoped n-type bismuth telluride, getting a high ZT at 130 °C of 0.92 compared to 0.68 for the pristine. The sample was simply prepared by mixing via agar and mortar, leading to a high ZT reached through improving the Seebeck coefficient parameter rather than electrical conductivity.
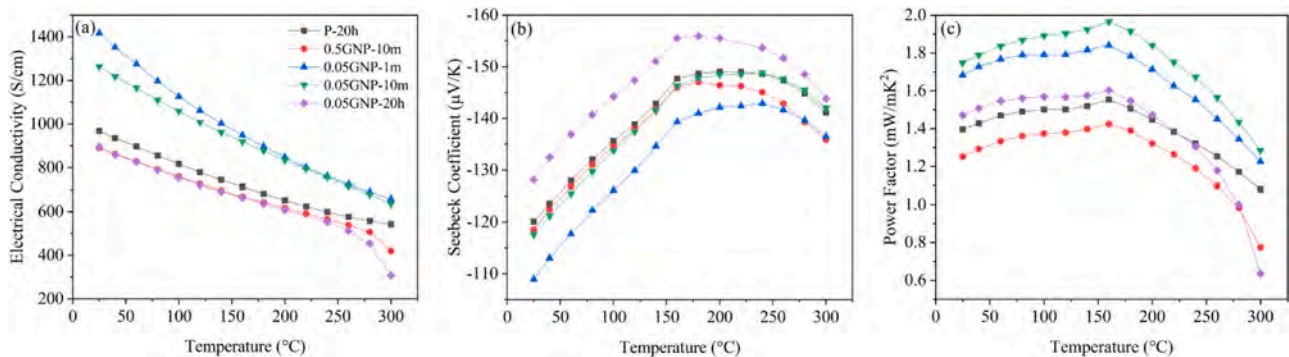

Fig. 9. (a) Electrical conductivity, (b) Seebeck coefficient, and (c) power factor trends for the pristine and GNP- Bi$_2$Te$_{2.7}$Se$_{0.3}$ composite samples.
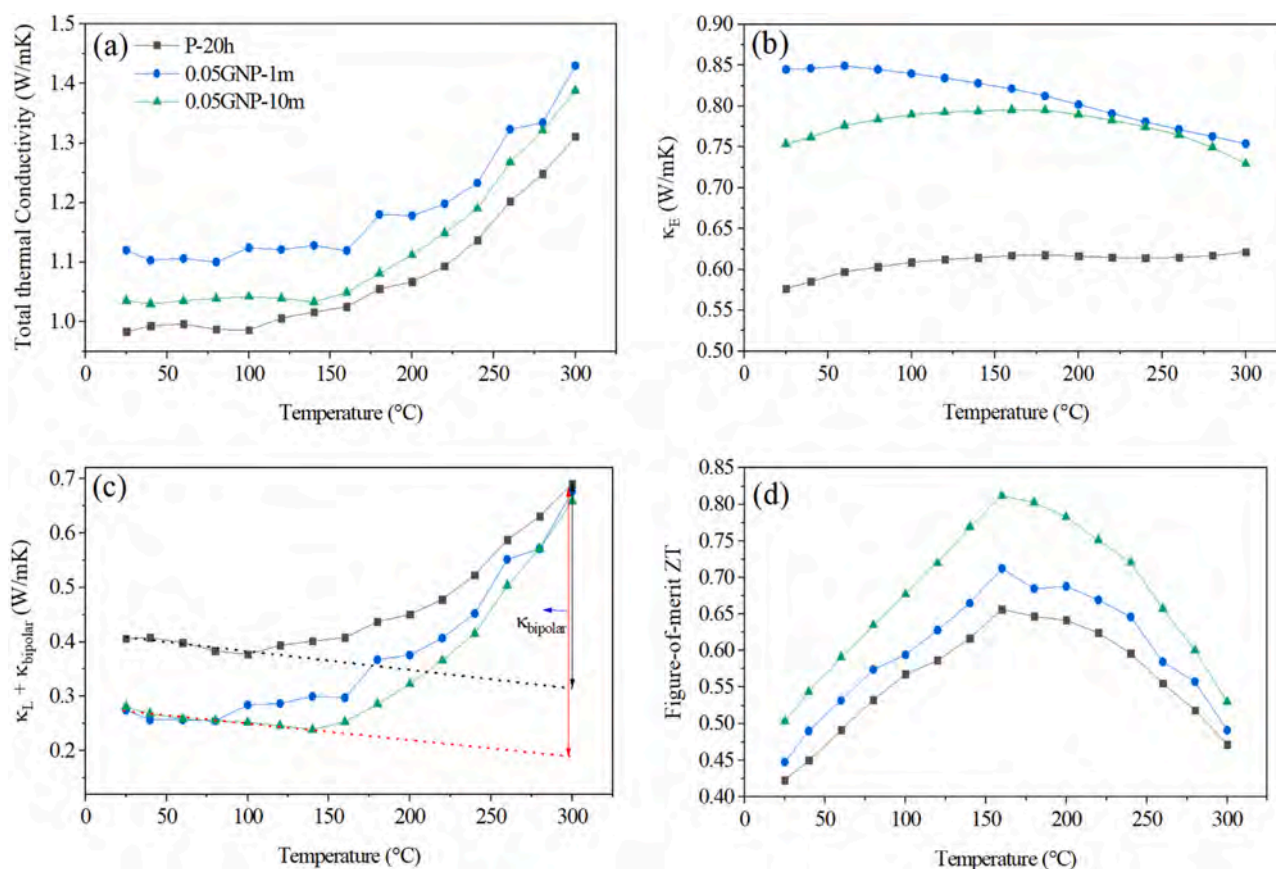
Fig. 10. (a) Total thermal conductivity, (b) electronic thermal conductivity, (c) lattice and bipolar thermal conductivities and (d) ZT for the pristine and optimized GNP-Bi$_2$Te$_{2.7}$Se$_{0.3}$ samples.

4. Conclusion

Graphene-Bi$_2$Te$_{2.7}$Se$_{0.3}$ composites were prepared through ball milling and spark plasma sintering techniques. In order to study the effect of the GNPs structural integrity on the thermoelectric properties, GNPs were added at different times (last 1 min, last 10 mins and for 20 hrs) to different GNP-Bi$_2$Te$_{2.7}$Se$_{0.3}$ samples containing either 0.05 or 0.5 wt% GNP. The average grain size of the as milled powders was estimated from the TEM analysis to be in 17–19 nm range with no grains above 50 nm. After consolidation using SPS, the grain size increases to the range of 50–120 nm. SEM revealed GNP nanosheets in the samples of short GNP milling time (1 and 10 min), but not in the 20 h milled sample. Raman Spectroscopy showed that (i) longer milling time of GNP increases milling-induced structural defects, (ii) milling GNPs for one-minute preserves its structure without exfoliation, (iii) increasing the milling time enhances the exfoliation and reduces agglomeration only in the lower concentration of 0.05 wt%, and (iv) the structural integrity of the GNPs breaks down with long hours of milling explaining why no nanosheets were observed in the SEM analysis. These observations had a significant effect on the thermoelectric properties. The electrical conductivity of higher GNP concentration was low due to the agglomeration and increased scattering of charge carriers. On the other hand, decreasing the milling time of GNPs enhanced the electrical conductivity as it preserves the GNP's structure and its high electrical conductivity. Low structural integrity and high defects improved the Seebeck coefficient as the milling time of GNPs increased. The thermal conductivity of the samples was dominated by the electronic part due to the high electrical conductivity of the optimized samples with less agglomeration. However, a noticeable reduction of the lattice thermal conductivity was observed due to the enhanced scattering at the new interfaces. As a result, GNP addition improved the

ZT value in the composite samples compared to pristine Bi$_2$Te$_{2.7}$Se$_{0.3}$. The optimum sample of low graphene concentration of 0.05 wt% added during the last 10 min of mechanical milling improved the ZT at room temperature to 0.5 (19% higher than pristine) and at 160 °C to 0.81 (25% higher than pristine) due to the preserved structural integrity of graphene with low agglomeration.

CRediT authorship contribution statement

Farah M. El-Makaty: Carried out the experimental work, wrote the first draft of the manuscript. **K. Andre Mkhoyan:** Analyzed the TEM results and contributed to the discussion and writing of the manuscript. **Khaled M. Youssef:** Is responsible for the conceptualization of the whole study, writing the manuscript, validating the results, performing the nanostructure analysis and the thermoelectric properties analysis, managing and coordinating responsibility for the research activity planning and execution.

Declaration of Competing Interest

The authors declare that they have no known competing financial interests or personal relationships that could have appeared to influence the work reported in this paper.

Acknowledgements

References

[1] A.H. Li, M. Shahbazi, S.H. Zhou, G.X. Wang, C. Zhang, P. Jood, G. Peleckis, Y. Du, Z.X. Cheng, X.L. Wang, Y.K. Kuo, Electronic structure and thermoelectric properties of bi2te3 crystals and graphene-doped bi2te3, Thin Solid Films 518 (2010) e57–e60, https://doi.org/10.1016/j.tsf.2010.03.124

[2] H. An, M. Pusko, D. Chun, S. Park, J. Moon, In-situ synthesis of flexible hybrid composite films for improved thermoelectric performance, Chem. Eng. J. 357 (2019) 547–558, https://doi.org/10.1016/j.cej.2018.09.200

[3] I.T. Witting, T.C. Chasapis, F. Ricci, M. Peters, N.A. Heinz, G. Hautier, G.J. Snyder, The thermoelectric properties of bismuth telluride, Adv. Electron. Mater. 5 (2019) 1800904, https://doi.org/10.1002/aelm.201800904

[4] M. Hong, Z.-G. Chen, J. Zou, Fundamental and progress of bi2te3-based thermoelectric materials, Chin. Phys. B 27 (2018) 048403, https://doi.org/10.1088/1674-1056/27/4/048403

[5] W.H. Shin, K. Ahn, M. Jeong, J.S. Yoon, J.M. Song, S. Lee, W.S. Seo, Y.S. Lim, Enhanced thermoelectric performance of reduced graphene oxide incorporated bismuth-antimony-telluride by lattice thermal conductivity reduction, J. Alloy. Compd. 718 (2017) 342–348, https://doi.org/10.1016/j.jallcom.2017.05.204

[6] K. Tae Kim, Y. Seong Eom, I. Son, Fabrication process and thermoelectric properties of cnt/bi2(se,te)3 composites, J. Nanomater. 2015 (2014).

[7] M.Y. Kim, Y.H. Yeo, D.H. Park, T.S. Oh, Thermoelectric characteristics of the (bi,sb)2(te,se)3 nanocomposites processed with nanoparticle dispersion, Ceram. Int. 38 (2012) S529–S533, https://doi.org/10.1016/j.ceramint.2011.05.069

[8] G. Yang, L. Li, W.B. Lee, M.C. Ng, Structure of graphene and its disorders: a review, Sci. Technol. Adv. Mater. 19 (2018) 613–648, https://doi.org/10.1080/14686996.2018.1494493

[9] J.I. Kim, E.S. Lee, J.Y. Kim, S.M. Choi, K.H. Lee, W.S. Seo, Erratum: Borderud SP, Li Y, Burkhalter JE, Sheffer CE and Ostroff JS. Electronic cigarette use among patients with cancer: Characteristics of electronic cigarette users and their smoking cessation outcomes. Cancer. doi: 10.1002/ cncr.28811, Cancer 121 (2015) 800, https://doi.org/10.1002/pssr.201308321

[10] C. Shen, S.O. Oyadiji, The processing and analysis of graphene and the strength enhancement effect of graphene-based filler materials: a review, Mater. Today Phys. 15 (2020) 100257, https://doi.org/10.1016/j.mtphys.2020.100257

[11] S. Wang, Y. Baocheng, Z. Houyang, Z. Shouren, C. Yan, F. Zhaochuan, Fracture behaviors of brittle and ductile 2d carbon structures under uniaxial tensile stress, Carbon 111 (2017) 486–492, https://doi.org/10.1016/j.carbon.2016.10.021

[12] K. Agarwal, V. Kaushik, D. Varandani, A. Dhar, B.R. Mehta, Nanoscale thermoelectric properties of bi2te3 – graphene nanocomposites: conducting atomic force, scanning thermal and kelvin probe microscopy studies, J. Alloy. Compd. 681 (2016) 394–401, https://doi.org/10.1016/j.jallcom.2016.04.161

[13] S. Kumar, S. Singh, P.K. Dhawan, R.R. Yadav, N. Khare, Effect of graphene nanofillers on the enhanced thermoelectric properties of Bi2Te3nanosheets: elucidating the role of interface in de-coupling the electrical and thermal characteristics, Nanotechnology 29 (2018) 135703, https://doi.org/10.1088/1361-6528/aaa99e

[14] B. Liang, Z. Song, M. Wang, L. Wang, W. Jiang, Fabrication and thermoelectric properties of graphene/Bi2Te3composite materials, J. Nanomater. 2013 (2013) 1–5, https://doi.org/10.1155/2013/210767

[15] H. Ju, J. Kim, Preparation and structure dependent thermoelectric properties of nanostructured bulk bismuth telluride with graphene, J. Alloy. Compd. 664 (2016) 639–647, https://doi.org/10.1016/j.jallcom.2016.01.002

[16] H. Ju, M. Kim, J. Kim, Preparation of graphene sheets into one-dimensionally nanostructured bulk bismuth telluride for enhancing thermoelectric power factor, J. Mater. Sci. Mater. Electron. 27 (2016) 3427–3434, https://doi.org/10.1007/s10854-015-4175-9

[17] K. Ahmad, C. Wan, M.A. Al-Eshaikh, A.N. Kadachi, Enhanced thermoelectric performance of Bi2Te3 based graphene nanocomposites, Appl. Surf. Sci. 474 (2019) 2–8, https://doi.org/10.1016/j.apsusc.2018.10.163

[18] M.S.T. Degen, E. Bron, U. König, G. Nénert, The highscore suite, Powder Diffr. 29 (2014) S13–S18.

[19] K.M. Youssef, R.O. Scattergood, K.L. Murty, C.C. Koch, Nanocrystalline al–mg alloy with ultrahigh strength and good ductility, Scr. Mater. 54 (2006) 251–256, https://doi.org/10.1016/j.scriptamat.2005.09.028

[20] L. Ruiz, M.J. Readey, Effect of heat treatment on grain size, phase assemblage, and mechanical properties of 3 mol% y-tzp, J. Am. Ceram. Soc. 79 (1996) 2331–2340, https://doi.org/10.1111/j.1151-2916.1996.tb08980.x

[21] Y. Zhang, H. Ma, B. Sun, B. Liu, H. Liu, L. Kong, B. Liu, X. Jia, X. Chen, Thermoelectric performance of graphene composited bisbte bulks by high pressure synthesis, J. Alloy. Compd. 715 (2017) 344–348, https://doi.org/10.1016/j.jallcom.2017.05.004

[22] C. Li, X. Qin, Y. Li, D. Li, J. Zhang, H. Guo, H. Xin, C. Song, Simultaneous increase in conductivity and phonon scattering in a graphene nanosheets/(bi2te3)0.2(sb2te3)0.8 thermoelectric nanocomposite, J. Alloy. Compd. 661 (2016) 389–395, https://doi.org/10.1016/j.jallcom.2015.11.217

[23] M. Bastwros, G.-Y. Kim, C. Zhu, K. Zhang, S. Wang, X. Tang, X. Wang, Effect of ball milling on graphene reinforced al6061 composite fabricated by semi-solid sintering, Compos. Part B Eng. 60 (2014) 111–118, https://doi.org/10.1016/j.compositesb.2013.12.043

[24] G. Gao, D. Liu, S. Tang, C. Huang, M. He, Y. Guo, X. Sun, B. Gao, Heat-initiated chemical functionalization of graphene, Sci. Rep. 6 (2016) 20034, https://doi.org/10.1038/srep20034

[25] I. Estrada, F. Robles-Hernández, R. Martínez-Sánchez, Materials characterization, A Green Method for Graphite Exfoliation Using a Mechanochemical Route (2015) 179–188, https://doi.org/10.1007/978-3-319-15204-2_18

[26] A. Liang, X. Jiang, X. Hong, Y. Jiang, Z. Shao, D. Zhu, Recent developments concerning the dispersion methods and mechanisms of graphene, Coatings 8 (2018) 33, https://doi.org/10.3390/coatings8010033

[27] J.-B. Wu, M.-L. Lin, P.-H. Tan, P.-H. Tan (Ed.), Raman spectroscopy of two-dimensional materials, Springer Singapore, Singapore, 2019.

[28] M. Wall (Ed.), T.F. Scientific, Thermo Fisher Scientific, USA, 2011.

[29] X. Dewen, X. Jingtao, L. Guoqiang, L. Zhu, S. Hezhu, T. Xiaojian, J. Jun, J. Haochuan, Synergistic optimization of thermoelectric performance in P-Type Bi0.48Sb1.52Te3/graphene composite, Energies 9 (4) (2016) 236–244.

[30] Y.B. Pottathara, H.R. Tiyyagura, Z. Ahmad, K.K. Sadasivuni, Graphene based aerogels: fundamentals and applications as supercapacitors, J. Energy Storage 30 (2020) 101549, https://doi.org/10.1016/j.est.2020.101549

[31] Y. Pan, U. Aydemir, F.-H. Sun, C.-F. Wu, T.C. Chasapis, G.J. Snyder, J.-F. Li, Self-tuning n-type Bi2(Te,Se)3/SiC thermoelectric nanocomposites to realize high performances up to 300 °C, Adv. Sci. 4 (2017) 1700259, https://doi.org/10.1002/advs.201700259

[32] S. Agrawal, M.K. Rai, Quiz page May 2015: crystalline nephropathy in an identical twin, Am. J. Kidney Dis. Off. J. Natl. Kidney Found. 65 (2015) 17–19.